The Nonlinear Study of Composite Plates Natural Frequency Using RNN-LSTM combined with Wavelet Transform Features

Wael A. Altabey

Department of Mechanical Engineering, Faculty of Engineering, Alexandria University, Alexandria, Egypt
Email: wael.altabey@gmail.com

***Abstract*—In this research, we discuss how we extract features related to natural frequency of Nonlinear Composite Plates (NCP) using a combination of Wavelet Transform (WT) and Artificial Intelligence (AI) algorithms. The nonlinearity is represented in the plate geometry and Boundary Conditions (BCs). Our findings, which build on previous works by the authors, indicate that WT can effectively reflect the natural frequency features of NCP. However, we also noted that this approach can be quite complex, involving numerous calculations and iterations, which means it might not be ideal for quickly and accurately extracting natural frequency. To tackle this issue, we've developed a new AI model designed to learn from and test these results by extracting key natural frequency features that reveal crucial information about the NCP behavior. The AI model is based on a Recurrent Neural Network with Long Short-Term Memory (RNN-LSTM) blocks since the natural frequency datasets have a time-dependent and memory-dependent behavior. Our results strongly suggest that the proposed technique is a promising approach, especially for complex structures in varying environmental conditions.**

***Keywords*—Nonlinear Composite Plates (NCP), natural frequency, Wavelet Transform (WT), Recurrent Neural Network (RNN), Long Short-Term Memory (LSTM) blocks**

I. Introduction

Lately, there's been some exciting progress in modal analysis and vibration diagnostics, thanks in large part to the use of cutting-edge methods like deep learning and new signal processing techniques. These advancements have made it easier to keep an eye on structural integrity and improve predictive maintenance strategies. They also help a lot in spotting and predicting vibrational behavior in both mechanical and civil engineering structures, along with analyzing noise and vibration data [1–5].

The way composite structures behave under vibration has long been a go-to method for spotting defects in these materials. Over the past few decades, mode shapes have become crucial tools in Structural Health Monitoring (SHM). This involves looking at the vibration responses of composite structures for various types and locations of damage and analyzing the differences in vibration parameters. Recently, there's been a surge of interest in finding techniques to extract the natural frequencies of composite plates within the scientific community [6–10].

To determine mode shapes under various boundary conditions using an Iterative Elastic Support (IES), both numerical and experimental methods are necessary. Some researchers have focused on the vibrations of multi-span plates through a variety of approaches. For instance, in earlier studies, Meng *et al.* [11], Hong *et al.* [12], Runqiu *et al.* [13], Al-Tabey [14], and Chen *et al.* [15] utilized the Finite Strip Method (FSTM) as a popular semi-analytical approach to extract vibration responses from basalt Fiber Reinforced Polymer (FRP) laminated plates of varying thickness. He aimed to boost accuracy and cut down on the computational effort, which can be quite high due to numerous iterations, by merging his method with Artificial Neural Networks (ANNs) and Response Surface (RS) techniques. Bouadjadja *et al.* [16] looked at large deflections in composite cantilever beams from a theoretical angle, sticking with the Euler–Bernoulli model, and backed up their findings with some experiments. Cheng *et al.* [17] introduced a structure with frequency-variable characteristics for harvesting vibration energy using piezoelectric elements, relying on nonlinear magnetic and piecewise linear forces. They discussed what factors could influence the performance of this device through both theoretical and experimental findings. Wu *et al.* [18] applied the first-order shear deformation theory to examine how various parameters impact the nonlinear dynamic behavior of composite plates that are reinforced with a small amount of graphene. Guo *et al.* [19] came up with a complex equation for how graphene-reinforced composite cantilever structures behave, using first-order deformation theory. They also looked into how nonlinear factors impacted the dynamics of various vibration modes. Meanwhile, Viet *et al.* [20] studied how composite cantilever beams respond to concentrated loads, using Timoshenko beam theory. They discussed how temperature and layer count in the beams influenced their deformation. Jun *et al.* [21] applied

Manuscript received November 6, 2025; revised December 18, 2025; accepted February 9, 2026; published April 23, 2026.

third-order shear deformation theory along with a dynamic stiffness method to see how the length of laminated composite cantilever beams affects their free vibrations. Amabili *et al.* [22] came up with an improved third-order shear deformation theory to explore nonlinear vibrations in cantilever beams. They carried out experiments on large-amplitude vibrations and did some numerical simulations with self-healing cantilever beams. At the same time, Zhang *et al.* [23] set up a two-dimensional nonlinear dynamic system focusing on a symmetric cross-ply laminated composite cantilever structure, investigating how different excitation types affected nonlinear vibrations and identifying chaotic behavior in the system they developed. Liu and Sun [24] used Galerkin discretization to derive a nonlinear system for a cantilever beam, taking third-order shear effects into account and discovering chaotic responses via numerical simulations. Guo *et al.* [25] looked at how third-order shear deformation can be used to model a big macrofiber composite cantilever. They discovered that this setup could show nonlinear vibration responses when faced with various disturbances. Meanwhile, Zhang *et al.* [26] studied bistable asymmetric deployable composite laminated cantilever structures, creating a two-dimensional nonlinear dynamic system. Their research showed that changes in amplitude and frequency of the foundation can lead to chaotic snap-through vibrations in these cantilevers. Teymouri and Biglari [27] introduced Green's functions for stress and displacement caused by wave propagation in a sandwich panel, which has transversely isotropic face sheets and an aluminum foam core. Lastly, Sun *et al.* [28] designed a composite laminated cantilever structure, focusing on a two-dimensional dynamic system while considering third-order shear effects. They highlighted the significance of analyzing vibrations in composite laminated cantilever beams using multi-dimensional systems and succeeded in controlling the limit cycle responses of the structure.

When it comes to deep Convolutional Neural Networks (CNN), they typically overlook the sequential dependencies found in time-series data such as structures vibration behavior data. So, to handle sequential data, we usually turn to deep sequential models. That's where Recurrent Neural Network (RNN) come in—they're specifically designed for this kind of data. RNN can remember information from previous inputs and link it to target vectors using their internal memory. But a downside is the vanishing gradient problem that crops up during backpropagation with gradient-based optimization in deeper layers, making it tough for a standard RNN to grasp long-term dependencies. A popular fix for this is the Long Short-Term Memory (LSTM) architecture [14, 15], which adds gate activation vectors to help tackle that vanishing gradient issue.

Another option we have is the Gated Recurrent Unit (GRU) neural network. Its structure is quite similar to LSTM but comes with fewer hyperparameters to manage, which can be an advantage. Recently, RNN and their variants have really gained traction as part of data-driven deep learning models. Then, Qi *et al.* [29] explored in their studythe complex nonlinear spatiotemporal behavior of a cantilever micro nanomanipulator, employing a radial basis function RNN. They were pretty successful in mapping out the model of the cantilever structure they were investigating. Subramanian and Mahadevan [30] combined Bayesian state estimation with a deterministic RNN to predict the vibrations of a nonlinear air cycle machine, demonstrating how this kind of forecasting works within a dynamic discrete system. Teng and Zhang [31] developed a new multi-step deep neural network model that integrates CNN, LSTM networks, and a multi-step strategy to analyze nonlinear dynamic systems and forecast their future states. When they stacked their model against other multi-step DNNs, it outperformed them in predicting chaotic vibration dynamics. Cestnik and Abel [32] investigated how well LSTM and GRU could forecast three chaotic systems, discovering that both were effective at estimating the dynamic characteristics of nonlinear systems. Huang *et al.* [33] introduced a new prediction model featuring a dual-stage attention-based RNN and GRU, which excelled at capturing periodicity and long-range dependencies in sequence data. Uribarri and Mindlin [34] employed LSTM to forecast chaotic time series from a Rössler system. Dudukcu *et al.* [35] rolled out a new temporal convolutional RNN model and validated its accuracy across various chaotic systems, including the Lorenz and Rössler systems. Sangiorgio *et al.* [36] experimented by adding different levels of noise to chaotic systems, using multiple prediction models to make forecasts, and found that LSTM performed exceptionally well, even without teacher forcing, in managing complex systems and noise. Sun *et al.* [37] set up a five-degree-of-freedom Duffing system and proposed an LSTM encoder-decoder neural network for predictions, showcasing its capability to forecast chaotic vibrations in discrete systems. In a similar vein, Wang *et al.* [38] developed a data-driven model that combined CNN and convolutional LSTM, confirming its accuracy and efficiency in predicting chaotic vibrations in a micro-beam system.

In this research, The RNN-LSTM is selected because the natural frequency datasets have a time-dependent and memory-dependent behavior, instead of use another common algorithms such CNN that are fundamentally designed for spatial/image data rather than time-series data. Fig. 1 show the proposed framework to predict the natural frequency of Nonlinear Composite Plates (NCP). As shown in the figure the natural frequency features of the plate will be extracted by using WT method to create training data for the RNN-LSTM. The trained RNN-LSTM will be used to predict the natural frequency for different levels of IES (so, varying elastic restraint coefficient (K_T), and skew in one of side (ϕ) values). While also looking at four different BCs scenarios for the plate edges such as SSSS, CCCC, SSFF, and CCFF to efficiently predict the natural frequency.

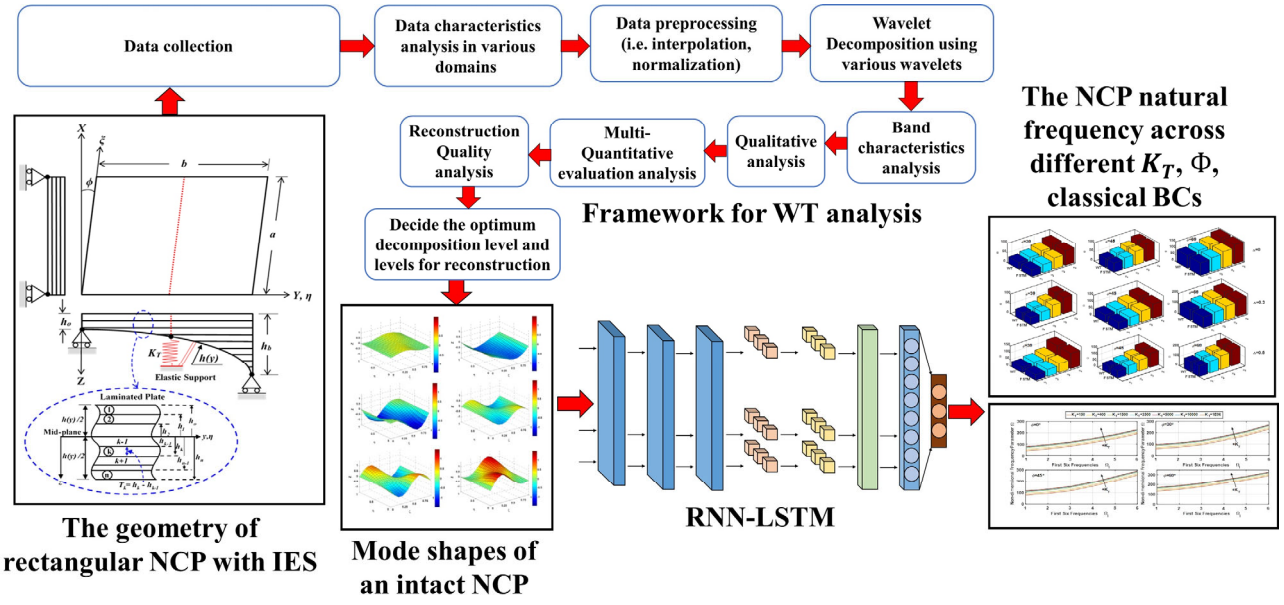

Fig. 1. The proposed framework in current research.

II. Materials and Methods

A. Model Overview

The plate is rectangular which made from Basalt Fiber Reinforced Polymer (BFRP) using five symmetrical layers arranged at a stacking angle of [45°/−45°/45°/−45°/45°], as illustrated in Fig. 2.

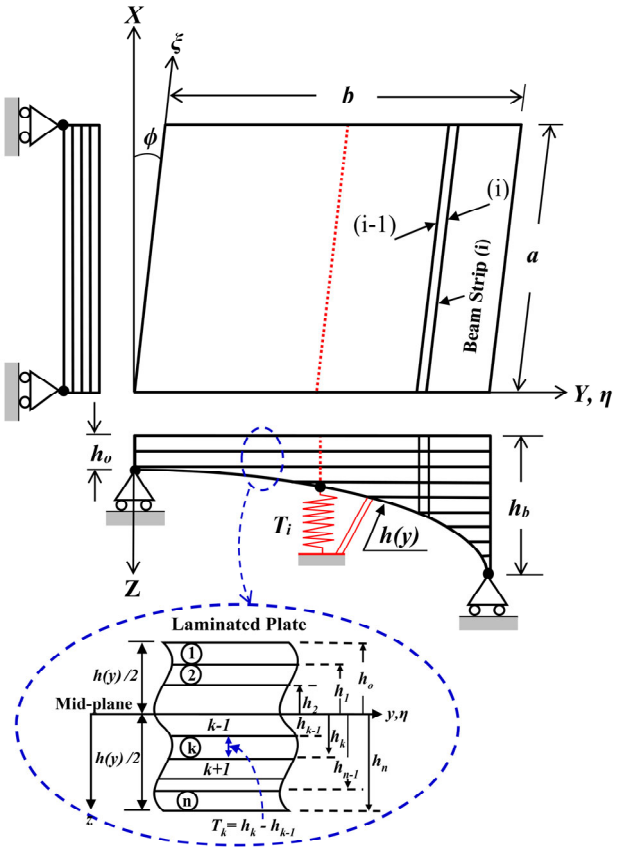

Fig. 2. The geometry of rectangular NCP with IES.

Table I shows the elastic and shear modulus values for the composite plate material.

To analyze the vibration behavior of the plate system depicted in Fig. 2, we utilize the normalized partial differential equation, assuming classical deformation theory.

TABLE I. Material Property

E_{11} (GPa)	E_{22} (GPa)	υ_{12}	υ_{21}	G_{12} (GPa)	G_{21} (GPa)	ρ kg/m^3
96.74	22.55	0.3	0.6	10.64	8.73	2700

In this context, we define the plate deflection in Eq. (1) as $w_o(x, y, t)$ [39].

$$D_{11}W_{xxxx} + 4D_{16}W_{xxxy} + 2(D_{12} + 2D_{66})W_{xxyy} + 4D_{26}W_{xyyy} + D_{22}W_{yyyy} = -m_o\frac{h(y)}{h_o}W_{tt} \quad (1)$$

where $W_{xxxx} = \frac{\partial^4 w_o}{\partial x^4}$, $W_{yyyy} = \frac{\partial^4 w_o}{\partial y^4}$, $W_{xxyy} = \frac{\partial^4 w_o}{\partial x^2 \partial y^2}$, $W_{xxxy} = \frac{\partial^4 w_o}{\partial x^3 \partial y}$, $W_{xyyy} = \frac{\partial^4 w_o}{\partial x \partial y^3}$, $D_{ij} = \frac{1}{3}\frac{h^3(y)}{h_o^3}$,

$$\sum_{k=1}^{n}\left[\bar{Q}_{ij}\right]_k (h_{ok}^3 - h_{ok-1}^3),\ i, j = 1,2,3,\cdots \quad (2)$$

In Eq. (2), the transformed reduced stiffness coefficients $\bar{Q}_{ij}$ of the lamina in terms of engineering notations can be described in Eq. (3) like this:

$$Q_{ij} = \begin{bmatrix} Q_{11} & Q_{12} & Q_{13} \\ Q_{12} & Q_{22} & Q_{23} \\ Q_{13} & Q_{23} & Q_{66} \end{bmatrix} = \begin{bmatrix} \frac{E_{11}}{(1-\nu_{12}\nu_{21})} & \frac{\nu_{21}E_{11}}{(1-\nu_{12}\nu_{21})} & 0 \\ \frac{\nu_{21}E_{11}}{(1-\nu_{12}\nu_{21})} & \frac{E_{22}}{(1-\nu_{21}\nu_{12})} & 0 \\ 0 & 0 & G_{12} \end{bmatrix} \quad (3)$$

We introduce non-dimensional variables ξ and η related to the skew coordinate system (u, v, ϕ) with $u = xsec(\phi)$, $v = y - xtan(\phi)$, and $\xi = \frac{u}{a}$, $\eta = \frac{v}{b}$. After some derivation, we can express the governing equation Eq. (4) as follows:

$$\begin{aligned}
&\Psi_1 h^3(\eta)\tfrac{1}{a^4}W_{\xi\xi\xi\xi} - 4\beta\Psi_3(\sin\phi)h^3(\eta)W_{\xi\xi\xi\eta} \\
&+\nu\beta^4\Psi_2(\cos^2\phi)\tfrac{\partial^2 h^3(\eta)}{\partial\eta^2}W_{\xi\xi} \\
&+2\beta^2\Psi_2(\cos^2\phi)\tfrac{\partial h^3(\eta)}{\partial\eta}W_{\xi\xi\eta} \\
&+2\beta^2\Psi_2 h^3(\eta)(3\sin^2\phi+\cos^2\phi)W_{\xi\xi\eta\eta} \\
&+2\beta^4(\cos^2\phi)\tfrac{\partial h^3(\eta)}{\partial\eta}W_{\eta\eta\eta} \\
&-2\nu\beta^3\Psi_4(\sin\phi\cos^2\phi)\tfrac{\partial^2 h^3(\eta)}{\partial\eta^2}W_{\xi\eta} \\
&-4\beta^3\Psi_4(\sin\phi)h^3(\eta)W_{\xi\eta\eta\eta} \\
&+\beta^4(\nu\tan^2\phi+1)(\cos^4\phi)\tfrac{\partial^2 h^3(\eta)}{\partial\eta^2}W_{\eta\eta} \\
&+\beta^4 h^3(\eta)W_{\eta\eta\eta\eta} \\
&-4\beta^3\Psi_4(\sin\phi\cos^2\phi)\tfrac{\partial h^3(\eta)}{\partial\eta}W_{\xi\eta\eta} \\
&=-\Omega^2 h(\eta)h_o^2(\cos^4\phi)W_{tt}
\end{aligned} \tag{4}$$

where $\Psi_1 = \frac{D_{11}}{D_{22}}$, $\Psi_2 = \frac{(D_{12}+2D_{66})}{D_{22}}$, $\Psi_3 = \frac{D_{16}}{D_{22}}$, $\Psi_4 = \frac{D_{26}}{D_{22}}$.

In this work, we look at how we model the BCs in both the x and y directions using different combinations of classical BCs. Since our main focus here is on the IES conditions, we'll dive deeper into those. For the numerical analysis, we checked out four classical BCs setups: SSSS, CCCC, SSFF, and CCFF, which we can see illustrated in Fig. 3. We can find the parameters for these BCs in Table II.

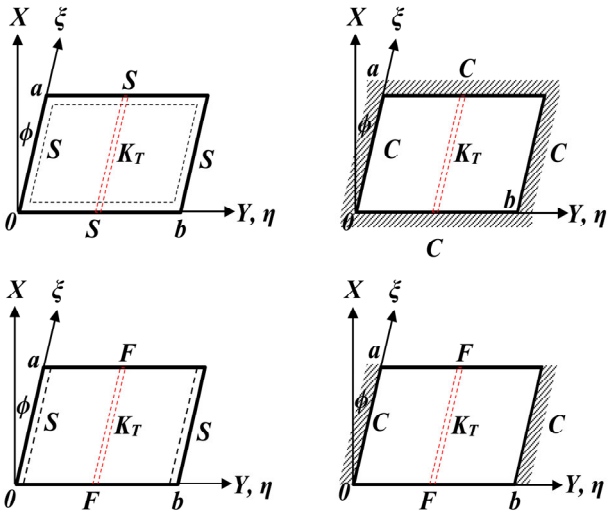

Fig. 3. Different combinations of classical BCs.

TABLE II. THE BCS PARAMETERS LIST

No.	Type	The Boundary Conditions
1	Simply supported edges	$w_o\|_{\xi=0,1} = 0, \frac{1}{a^2}\frac{\partial^2 w_o}{\partial\xi^2}\Big\|_{\xi=0,1} = 0$ $w_o\|_{\eta=0,1} = 0, \frac{1}{b^2}\frac{\partial^2 w_o}{\partial\eta^2}\Big\|_{\eta=0,1} = 0$
2	Clamped supported edges	$w_o\|_{\xi=0,1} = 0, \frac{1}{a}\frac{\partial w_o}{\partial\xi}\Big\|_{\xi=0,1} = 0$ $w_o\|_{\eta=0,1} = 0, \frac{1}{b}\frac{\partial w_o}{\partial\eta}\Big\|_{\eta=0,1} = 0$
3	Free edges	$\frac{1}{a^3}\frac{\partial^3 w_o}{\partial\xi^3}\Big\|_{\xi=0,1} = 0, \frac{1}{a^2}\frac{\partial^2 w_o}{\partial\xi^2}\Big\|_{\xi=0,1} = 0$ $\frac{1}{b^3}\frac{\partial^3 w_o}{\partial\eta^3}\Big\|_{\eta=0,1} = 0, \frac{1}{b^2}\frac{\partial^2 w_o}{\partial\eta^2}\Big\|_{\eta=0,1} = 0$
4	IES at $y = b/2$	$K_T w_o = -2\Psi_3\frac{\partial^3 w_o}{\partial x^3} - \frac{\partial^3 w_o}{\partial y^3} - \Psi_5\frac{\partial^3 w_o}{\partial x^2\partial y} - 4\Psi_4\frac{\partial^3 w_o}{\partial x\partial y^2}$ $\frac{\partial w_o}{\partial y}\Big\|_{\eta=1^-/2} = \frac{\partial w_o}{\partial y}\Big\|_{\eta=1^+/2}$ where $K_T = \frac{T_b/2b^3}{D_{22}}$, $\Psi_5 = \frac{(D_{12}+4D_{66})}{D_{22}}$

B. WT to Compute NCP Natural Frequency

This part discusses how we extract the mode shapes of the NCP using the WT method, while tweaking the frequency parameter. To get more precise results, we optimize this frequency parameter by minimizing the WT entropy.

1) Continuous Wavelet Transform (CWT)

The CWT for short, is a technique that works by convolving a data sequence with a set of wavelets created through continuous scaling and shifting of a base function known as the Mother Wavelet (MW), $\psi(t)$ [40]. By translating the wavelet, we can localize it in time across the input signal, $x(t)$, effectively smoothing it out over its entire length. Scaling changes the size of the wavelet, letting we analyze the data at different resolutions.

When we stretch the wavelet, it's great for spotting slow changes in the signal, while a compressed wavelet is better for quick, sharp shifts. This ability to look at multiple resolutions makes it possible to conduct detailed time-frequency analysis of the signal. But keep in mind, achieving a higher resolution can be demanding computationally and requires more memory, since it involves calculating wavelet coefficients for each scale and time step by multiplying the input signal with appropriately adjusted versions of the MW.

Mathematically speaking, the wavelet function $\psi(t)$ is scaled using a dilation parameter, *s*, and shifted along the time axis by a translation parameter, τ as Eq. (5). These manipulations let the wavelet slide along the time line and adjust its scale to pick up on different features of the signal [41–44].

$$\psi_{s,\tau}(t) = \frac{1}{\sqrt{s}}\psi\left(\frac{t-\tau}{s}\right) \quad \tau \in \Re,\ S > 0 \tag{5}$$

Let's define $x(t)$ as the shape function response of the system, where t represents time. The CWT of a function $x(t) \in L^2(\Re)$ —which refers to the space of square-integrable functions on the real line—is noted as $W_{s,\tau}$ in Eq. (6). This is defined as follows:

$$W_{s,\tau} = \langle x(t), \psi_{s,\tau}(t)\rangle = \frac{1}{\sqrt{s}}\int_{\infty}^{-\infty} x(t)\cdot\psi^*\left(\frac{t-\tau}{s}\right)dt \tag{6}$$

The wavelet scale s and period τ help us tweak the frequency and the timing. $W_{s,\tau}$ indicates how much the wavelet $\psi_{s,\tau}(t)$ aligns with $x(t)$. Using the inverse CWT, we can regenerate the signal $x(t)$ Eq. (7) as shown here:

$$x(t) = \frac{1}{C_\psi}\int_{-\infty}^{+\infty}\int_{-\infty}^{+\infty} W_{s,\tau}\ \psi_{s,\tau}\ \frac{dsd\tau}{S^2} \tag{7}$$

As shown in Fig. 2, the equation for a single beam system responding freely in the ξ-direction can be represented in Eq. (8) as way:

$$x(t) = X_i(\xi)Y_i(\eta)e^{j\omega\tau} \tag{8}$$

The WT of Eq. (8) is Eq. (9):

$$\left|W_{s_0,\tau}\right| = \frac{\sqrt{s_0}}{2}X_i(\xi)Y_i(\eta).\psi^*(S_0\omega)e^{j\omega\tau} \tag{9}$$

Taking the logarithm of Eq. (9) results in Eq. (10):

$$\ln\left|W_{s_0,\tau}\right| = j\omega\tau + \ln\left(\frac{\sqrt{s_0}}{2}X_i(\xi)Y_i(\eta)|\psi^*(S_0\omega)|\right) \tag{10}$$

By looking at the slope of the straight line from the logarithm of the WT modulus, we can determine the system's natural frequency Eq. (11), expressed as:

$$Arg\left(W_{s_0,\tau}\right) = \omega\tau \ \Rightarrow\ \frac{d}{d\tau}Arg\left(W_{s_0,\tau}\right) = \omega \tag{11}$$

The plot of $\frac{d}{d\tau}Arg\left(W_{s_0,\tau}\right)$ stays constant over time and relates to the natural frequency ω. The Non-Dimensional Frequency Parameter (NDFP), represented as Ω, is defined in Eq. (12) as:

$$\Omega = \left(\frac{m_o h(\eta)\omega^2 a^4}{h_o D_{22}}\right)^{1/2} \tag{12}$$

2) The Mother Wavelet (MW) selection methodology

To start, we need to define the research problem by looking at existing literature on selecting the right wavelets. This will give us a clearer picture of how crucial WT are when it comes to detecting structural damage. In this review, we'll also provide an overview of different measures for choosing wavelets, specifically for analyzing structural dynamic responses. We'll delve into the theoretical side of wavelet analysis to better grasp the underlying math involved.

Additionally, to build a solid intuition about wavelet characteristics, we'll examine wavelet properties, which helps in understanding what's needed for effective wavelet analysis and highlights the differences among various wavelet types. Using the insights gained, we'll select some wavelet families based on data characteristics and past research as our initial candidates for wavelet basis, which we'll then use to break down the data.

Next, we'll analyze the band characteristics and energy distribution at each level to find the optimal Decomposition Level (DL). After that, we'll carry out quantitative analyses with different wavelets. Finally, we'll validate the technique by assessing noise levels, energy loss, recovery quality, and extracting damage features from both experimental and simulated data. We will then conduct a comparative analysis based on the quantitative metrics to guide our decision-making. We can see Fig. 4 for the practical strategy we propose and how we plan to execute this work.

The MW selection procedures shown in Fig. 4 are explained in detail and carried out step by step. This process includes collecting data, analyzing its characteristics, examining wavelet properties, assessing band characteristics, choosing the appropriate scale level, and conducting a multi-quantitative measures analysis. Finally, we evaluate how effective the framework is and

compare the results of the quantitative measures to pinpoint the best wavelet.

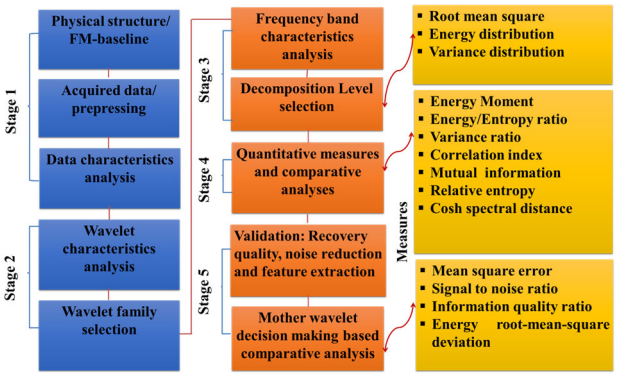

Fig. 4. Proposed guidelines for framework for selecting optimum MW.

3) *The wavelet drawbacks*

Wavelet transforms, especially the CWT, are known to be computationally intensive due to repeated calculations, increasing costs with signal length and decomposition levels, making them challenging for real-time systems; however, efficient methods like the optimized algorithms, and AI algorithms to mitigate these demands, particularly for the CWT [43, 44]. The reasons for high computational cost:

(1) Redundancy: CWT generates vast amounts of redundant data with high time-frequency resolution, demanding significant processing.
(2) Scaling & Shifting: The core CWT involves continuous scaling and shifting of the wavelet, requiring many integral computations.
(3) Increasing Levels: Deeper decomposition levels in DWT (for finer details) multiply the computational load.
(4) Comparison: CWT is generally more intensive than Fast Fourier Transform (FFT), though FFT lacks the time localization CWT offers.

In Section II.C, a novel RNN-LSTM architecture will be discussed to tackle this drawbacks in CWT.

C. *Artificial intelligence (AI) Algorithms*

Recently, deep learning, which involves using neural networks with several hidden layers, has become quite popular for tackling both ordinary and partial differential equations. As part of AI, these deep learning algorithms excel at handling complex, non-linear problems.

These networks are made up of interconnected nodes, often called neurons. Each neuron carries out a specific task on the input it gets, and then sends the result to the next nodes through their connections. Often, the output from one node becomes the input for one or more others, creating a multi-layered structure that can learn intricate patterns from the data.

Here, we're going to use the findings from Section II.B about the natural frequency of the NCP, which we got using the WT at chosen values of the K_T. We'll create training data from this, and then apply our trained RNN-LSTM model to predict the vibrational behavior of the NCP for different K_T values that weren't part of the training set.

1) *RNN- LSTM configuration*

In this study, we opted for the RNN-LSTM model over a traditional feedforward neural network to monitor bridge damage. This choice makes sense because the datasets from LiDAR sensors are both time-dependent and memory-dependent. The LSTM helps address the issue where the error signal used for training the network tends to diminish exponentially as we go further back in time within the RNN, illustrated in Fig. 5. This figure outlines the deep learning model we proposed to describe the restoring force in the hysteretic structural system of the bridge. Here, the input consists of the LiDAR sensor datasets, while the output focuses on detecting and classifying bridge damages [45].

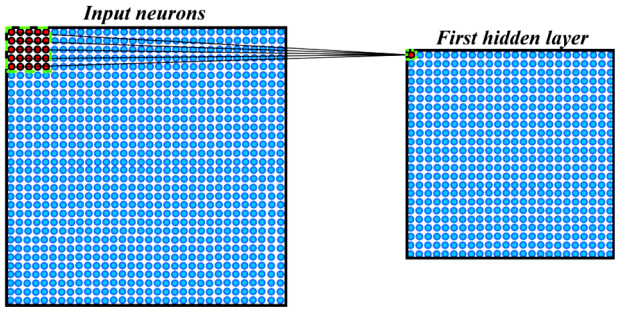

Fig. 5. The output creation from a rolls 5 × 5 filter around an input volume [45].

At each moment in a time series, an LSTM cell monitors a hidden vector and a memory vector, which help it manage its updates and outputs effectively. The output or activation for each LSTM cell is defined in Eq. (13) as follows:

$$h_t = \Gamma_o \cdot \tanh(C_t) \tag{13}$$

Where Γ_o is the output gate that controls the amount of information shared from memory (C_t), and here's how it's calculated in Eq. (14):

$$\Gamma_o = \sigma(W_o \cdot [h_{t-1}, X_t] + b_o) \tag{14}$$

So here's the deal: at any given time step (t), we have the input for the LSTM (X_t) and we're using the sigmoid activation function (σ). There's this weight matrix (W_o) that controls how the output gate operates. Then we've got h_{t-1}, which is the activation or hidden vector from the previous time step ($t-1$) taken from the last LSTM cell. Plus, there's a bias (b_o) that comes into play when we're figuring out the output.

Now, C_t represents the memory cell or vector that helps forget some of what's currently stored (C_{t-1}), pulls from the previous LSTM cell, and takes in new memory content ($\hat{C}_t$). We can define that in Eq. (15) as follows:

$$C_t = \Gamma_f \cdot C_{t-1} + \Gamma_u \cdot \hat{C}_t \tag{15}$$

Here's how the content of the new memory ($\hat{C}_t$) gets updated in Eq. (16):

$$\hat{C}_t = \tanh(W_c \cdot [h_{t-1}, X_t] + b_c) \quad (16)$$

So we have this weight matrix, W_c, and it pretty much controls how our new memory operates. Then there's the bias, b_c, which plays a role in shaping that memory.

In Eq. (15), we introduce Γ_f in Eq. (17), which helps figure out how much of the current memory we need to forget, hence the name forget gate. Then there's Γ_u in Eq. (18), another part that manages how much new info we actually add to the memory cell, which we refer to as the update/input gate. Since these gates are in charge of what's stored in memory, their values have to stay between zero and one. We accomplish that by using the sigmoid function in their setup. The next calculations will show we how that works.

$$\Gamma_f = \sigma(W_f \cdot [h_{t-1}, X_t] + b_f) \quad (17)$$

$$\Gamma_u = \sigma(W_u \cdot [h_{t-1}, X_t] + b_u) \quad (18)$$

In this configuration, W_f and W_u are the weight matrices that control how the forget gate and the input/update gate operate. Essentially, h_t and C_t are the outputs from the LSTM cell at time step t, which get sent to the next cell at time step $t+1$. If the LSTM cell at time step t generates this output, here's how we can calculate it in Eq. (19):

$$O_t = \text{softmax}(W_o \cdot h_t + b_o) \quad (19)$$

Fig. 6 illustrates the structure of the LSTM cell.

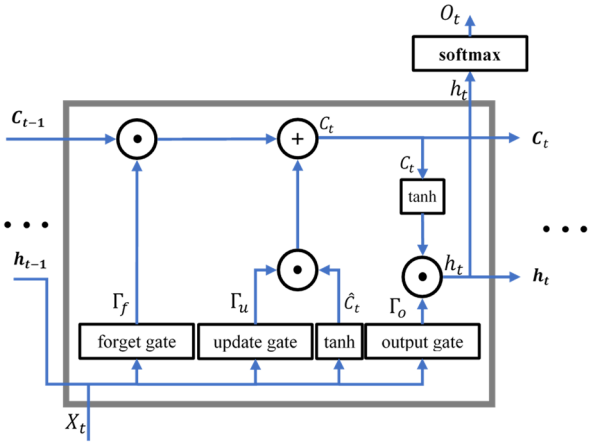

Fig. 6. An RNN-LSTM diagram (single block).

2) *Bidirectional LSTM*

Bidirectional architecture is essentially a flexible framework that can be integrated with any RNN model, LSTM included. In a biLSTM (or bidirectional LSTM) cell, we'll find two standard unidirectional LSTM cells working together: one analyzes past time steps and the other looks at future ones. Fig. 7 gives we a picture of how a biLSTM cell is structured.

At each time step, the biLSTM keeps track of two hidden states—one for the past and another for the future. This feature really boosts its performance for sequence-related tasks, like text classification. Speaking of that, we've categorized structural damage detection as a sequence classification problem in this study [46].

So, if a biLSTM cell generates an output at a particular time step, here's how we can compute it in Eq. (20):

$$O_t = softmax(W_o.[\vec{h}_t, \overleftarrow{h}_t] + b_o) \quad (20)$$

Here, $\vec{h}_t$ and $\overleftarrow{h}_t$ refer to the activations of the forward and backward biLSTM cells at time step t.

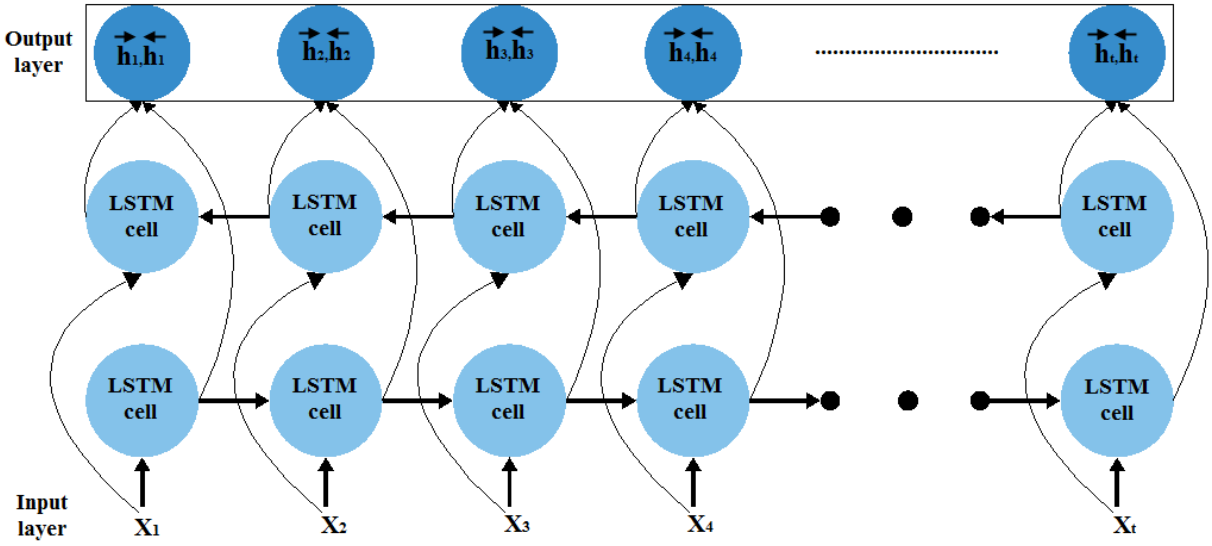

Fig. 7. The biLSTM structure.

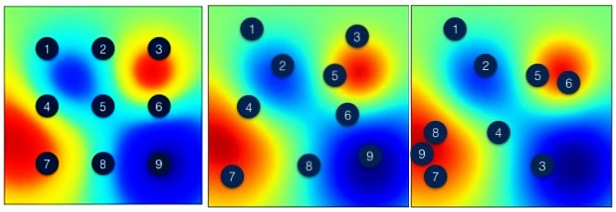

Fig. 8. The difference between (a) grid; (b) random; and (c) BGA optimization techniques.

3) *Bayesian Genetic Algorithms (BGA)*

There are several ways to make BGA work better for objective functions (f), like using Gaussian processes [47–49], random forests [50], and tree-structured Parzen estimators [51, 52]. If we check out Fig. 8, we'll see a comparison of the Grid search, Random search, and BGA Optimization methods for tuning the model's hyperparameters. The numbered circles show how well the model did using each method. It's interesting to note that while the Grid search covers broader areas, BGA optimization techniques can explore different combinations more intelligently and often find the best solutions with fewer tests. For this study, we decided to go with BGA techniques to speed up and enhance training.

III. Features Extraction

Generally, the features are coefficients or derived statistical measures that form a multi-scale, multi-resolution representation of the original data.

Fig. 9 displays the first six mode shapes that correspond to the natural frequencies of the intact NCP computed by Eq. (9) using WT approach.

In this study, we'll be looking at both the mode shapes components along with their natural frequencies to identify the NCP features. These will be used as inputs for the RNN-LSTM.

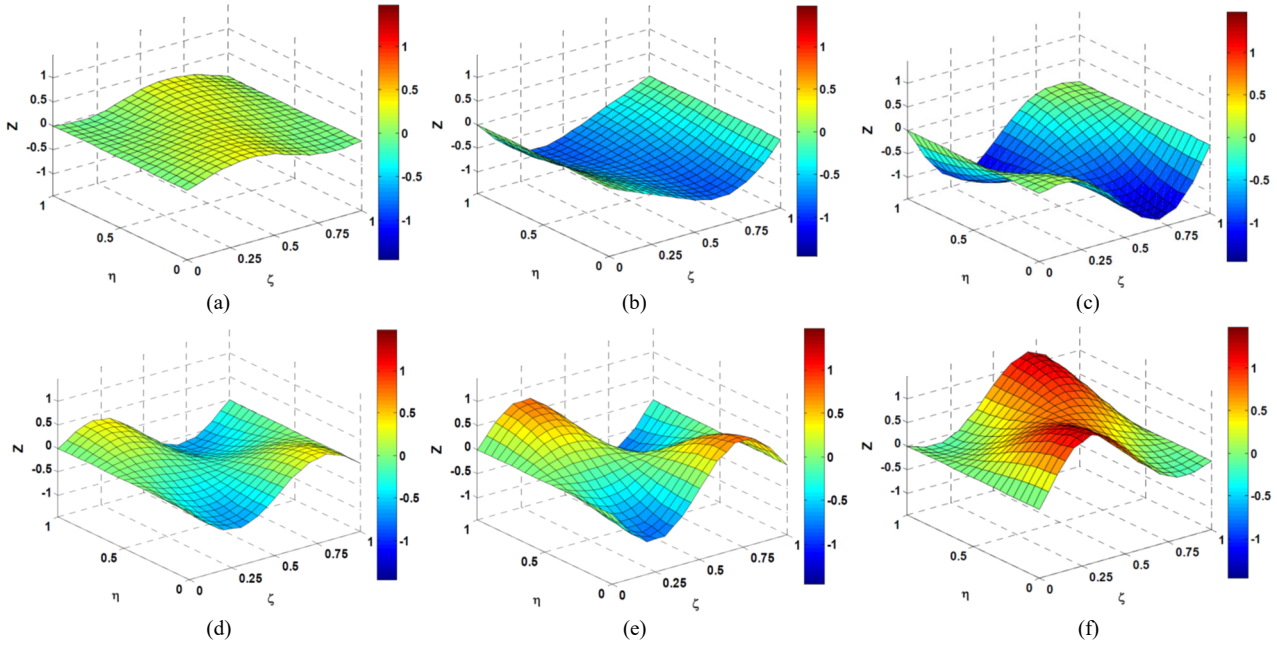

Fig. 9. The first six mode shapes of an intact NCP. (a) 1st mode; (b) 2nd mode; (c) 3rd mode; (d) 4th mode; (e) 5th mode; (f) 6th mode.

To estimate the NCP natural frequency at different K_T and skew angle ϕ values with four different BCs scenarios (SSSS, CCCC, SSFF, and CCFF) without getting bogged down in complex math, we came up with a new approach that uses an AI model based on RNN-LSTM. This model takes in NCP features at time t along with various K_T values and outputs the estimated natural frequency for each K_T, as illustrated in Fig. 10. We're confident that the architecture depicted in Fig. 10 is solid enough to learn from WT data and make accurate predictions, indicating good generalization.

The setup features an RNN-LSTM that starts with an input layer for the WT natural frequency data, incorporating the mode shapes of an intact NCP. This is followed by three 1D convolutional layers designed to eliminate data outliers, each with its own configurations: the first layer is set to 56×128, the second to 28×256, and the third to 14×512. Then, we include two sub-sampling LSTM layers, sized at 14×512 and 7×512. Afterward, we flatten all the 2D arrays from the pooled feature maps into a single long vector containing 25,088 elements. The output layer uses a softmax activation function to predict the NCP natural frequency across different K_T datasets. It's also important to note that while both the RNN and CNN models share similar architectures, they differ in the feature extraction areas near the input layer. We evaluate both the cost and accuracy of these models, checking the test set accuracy before and after training. To speed up training and improve accuracy, we used the BGA technique.

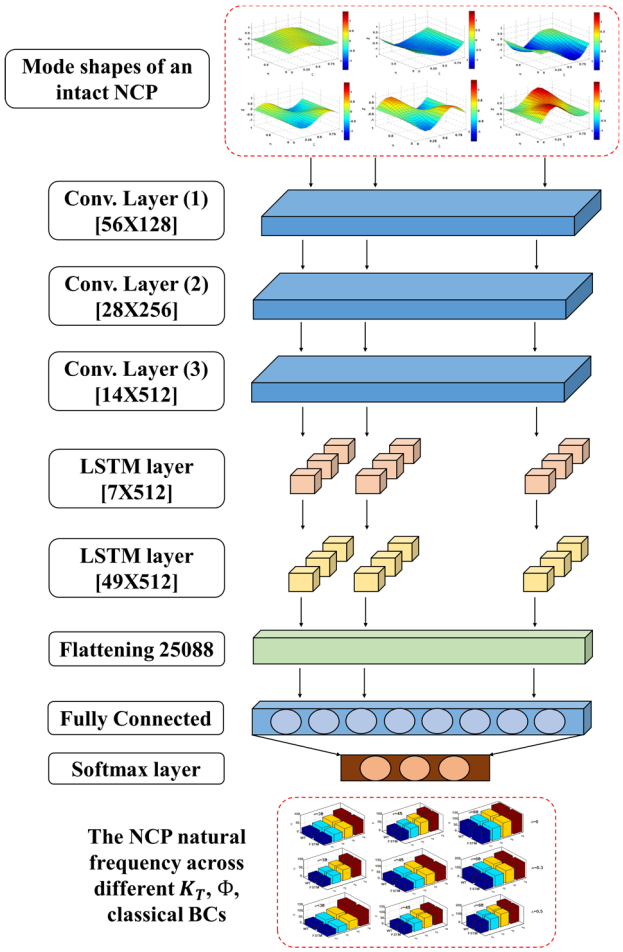

Fig. 10. The AI network that includes three 1-D convolutional layers, full connection layers, two sub-sampling LSTM layers, and a softmax layer.

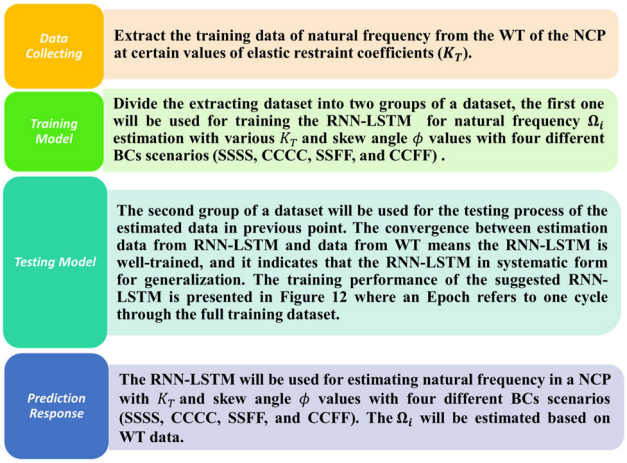

Fig. 11. The steps of RNN-LSTM training to predict NCP (Ω_i).

In this study, we chose the Mean Square Error (MSE) to fine-tune the network parameters, like weights and biases, across the different layers. During training, we utilize the features from multiple positions over time to tweak those parameters, especially as the hidden layer numbers shift based on training outcomes. After running several tests, we found that the network produces good results, and we wrap up the training once the MSE stabilizes at a low level. We can see the RNN-LSTM setup along with the training and testing model functions in Fig. 11, the RNN training performance in Fig. 12, and the key training parameters are detailed in Table III. Lastly, the steps involved in the MATLAB code for RNN training and evaluation are outlined in Algorithm 1.

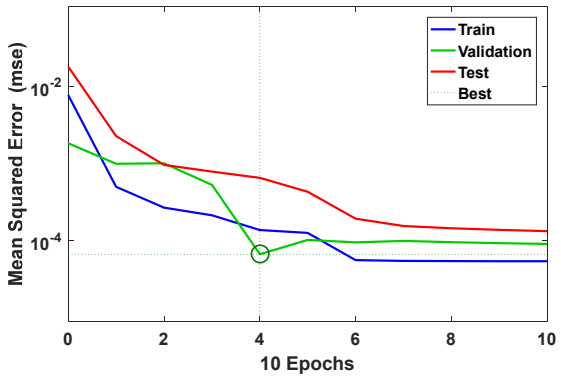

Fig. 12. RNN training performance.

TABLE III. RNN KEY PARAMETERS

Training Time	Gauge	Training Rate	Attenuation Factor
75 s	36	10^{-4}	10^{-6}

Algorithm 1: Training, and Testing of Proposed RNN

1: **input:** d: Ω_i dataset, I: K_T and ϕ W: Network parameter matrix weight w_{ij} and bias b_i
2: **output:** score of RNN trained model on the dataset to predict Ω_i for various K_T and ϕ
3: **let** fbe the feature set 3d matrix
4: **for** i in the dataset **do**
5: **let** f_i, be the feature set matrix of sample l
6: **for** j in i **do**
7: $V_i \leftarrow vectorize_{(j,w)}$
8: **append** V_i to f_i
9. **append** f_i to f
10: $f_{train}, f_{test}, l_{train}, l_{test} \leftarrow$ the split feature set and prediction into train subset and test subset
11: M ←RNN (f_{train}, l_{train})
12: score ← evaluation (l, , l_{test}, M)
13: **return** score
14: **end for**
15: **end for**

IV. RESULT AND DISCUSSION

This research focuses on a new AI designed model to predict the natural frequency of NCP. It considers nonlinear geometry of variable thickness profile ($h(y)$) and skew in one of side (ϕ), and nonlinear elastic support in the plate middle (IES) with a different elastic restraint coefficient (K_T). While also looking at four different BCs scenarios for the plate edges such as SSSS, CCCC, SSFF, and CCFF. The plate is rectangular which made from BFRP using five symmetrical layers arranged at a stacking angle of [45°/−45°/45°/−45°/45°],

We start by looking at some key findings from the existing research. After that, we present an analysis of the natural frequency of the NCP with variable thickness profile ($h(y)$) and skew angle (ϕ), using the WT approach discussed in Section II. This analysis focuses on specific

values of the K_T, which represent IES conditions. We then use the results from the WT method to create training data for the RNN-LSTM.

The selection of RNN-LSTM since the natural frequency datasets have a time-dependent and memory-dependent behavior, instead of use another common algorithms such CNN that are fundamentally designed for spatial/image data rather than time-series data. The predictions from our RNN-LSTM model closely matched the WT results, suggesting that this proposed approach shows great promise.

Once the RNN-LSTM is trained, we use it to examine how different levels of IES (so, varying K_T and ϕ values) affect the natural frequencies of the NCP. This two-step method not only helps validate the WT approach but also provides a way to efficiently predict the natural frequency across a wider range of support conditions (SSSS, CCCC, SSFF, and CCFF).

A. Convergence Study and Accuracy

It's really important to line up the findings from this work with what's already out there in the literature to make sure the technique we've proposed is both accurate and dependable. In this part, we're using the WT method on a clamped-clamped (CCCC) skew plate that has a variable thickness. We're looking at an aspect ratio of $\beta = a/b = 0.5$, with taper ratio $\Delta = (h_b - h_o)/h_o, (h_o)$ set at $\Delta = (0,0.2,0.4,0.5)$, and skew angles of $\phi = (30°, 45°, 60°)$ (see Fig. 2).

Fig. 13 shows how the WT results behave as they converge, comparing them with findings from the Finite Strip Transition Matrix Method (FSTM) mentioned in Ref. [14]. This side-by-side comparison really highlights how accurate and consistent the WT method is in our study.

As we can see from the figure, the results from our WT method match up really well with those from other reliable methods reported in the Ref. [14], especially once convergence is reached. This really backs up the WT-based approach is trustworthy for looking at the natural frequency of NCP.

We can definitely see how some important geometric factors of ϕ, Δ, and β affect the natural frequency (Ω) parameter in NCP. In particular, as ϕ, Δ, and β go up, so does Ω, showing that these elements really impact how the plate responds dynamically.

B. Proposed Method Results

In this study, we used numerical computations based on the WT method to analyze the natural frequency of NCP. That said, the WT approach can be pretty complex, requiring a lot of calculations and iterations, which makes it less efficient for quick and precise vibration analysis. To tackle this issue, we developed a new RNN-LSTM model aimed at learning from the results we got with the WT method. This RNN-LSTM is specifically trained to pick up on and extract features of the natural frequency that highlight key details about the mode shapes of the NCP.

For our proposed method, we trained the model using data from just two $K_T = 50$ and $K_T = 750$. These were then used to calculate t the natural frequency (Ω) of NCP, which became the training set for the RNN-LSTM.

We calculated the Ω for various skew angles (ϕ), while keeping the aspect ratio at $\beta = 0.5$ and the taper ratio at $\Delta = 0.5$. This analysis considered four standard boundary conditions: SSSS, CCCC, SSFF, and CCFF, allowing us to examine how the skew angle impacts the natural frequencies.

Figs. 14 and 15 show a comparison between the Ω values calculated using WT and those predicted by the RNN-LSTM for $K_T = 50$ and $K_T = 750$under the four BCs. The findings indicate that the RNN-LSTM model achieves impressive prediction accuracy, confirming its potential for predicting vibration behavior in complex structural systems.

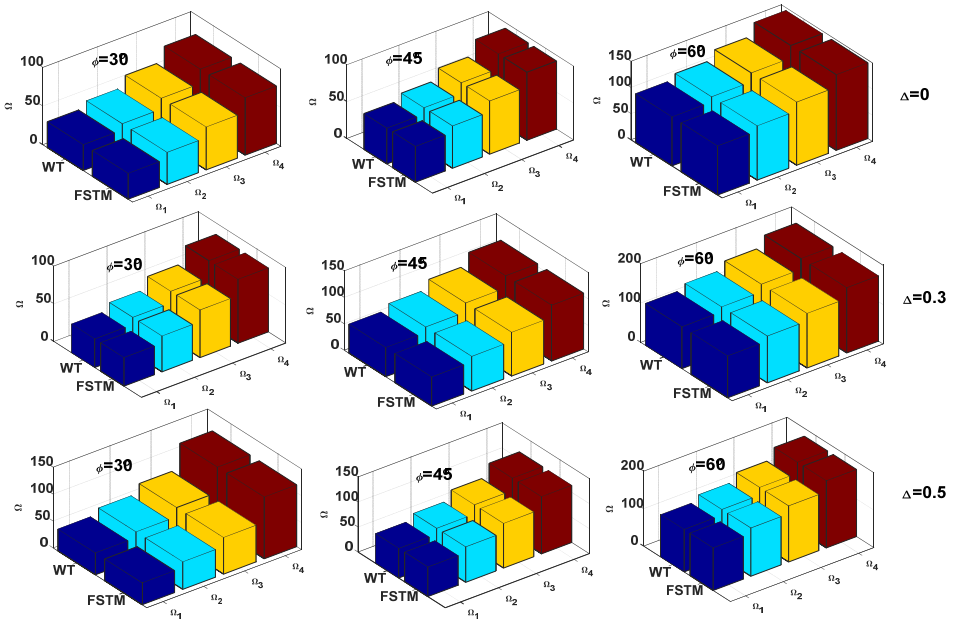

Fig. 13. Comparison between WT and FSTM results of the first four natural frequencies in CCCC NCP $\beta = 0.5$.

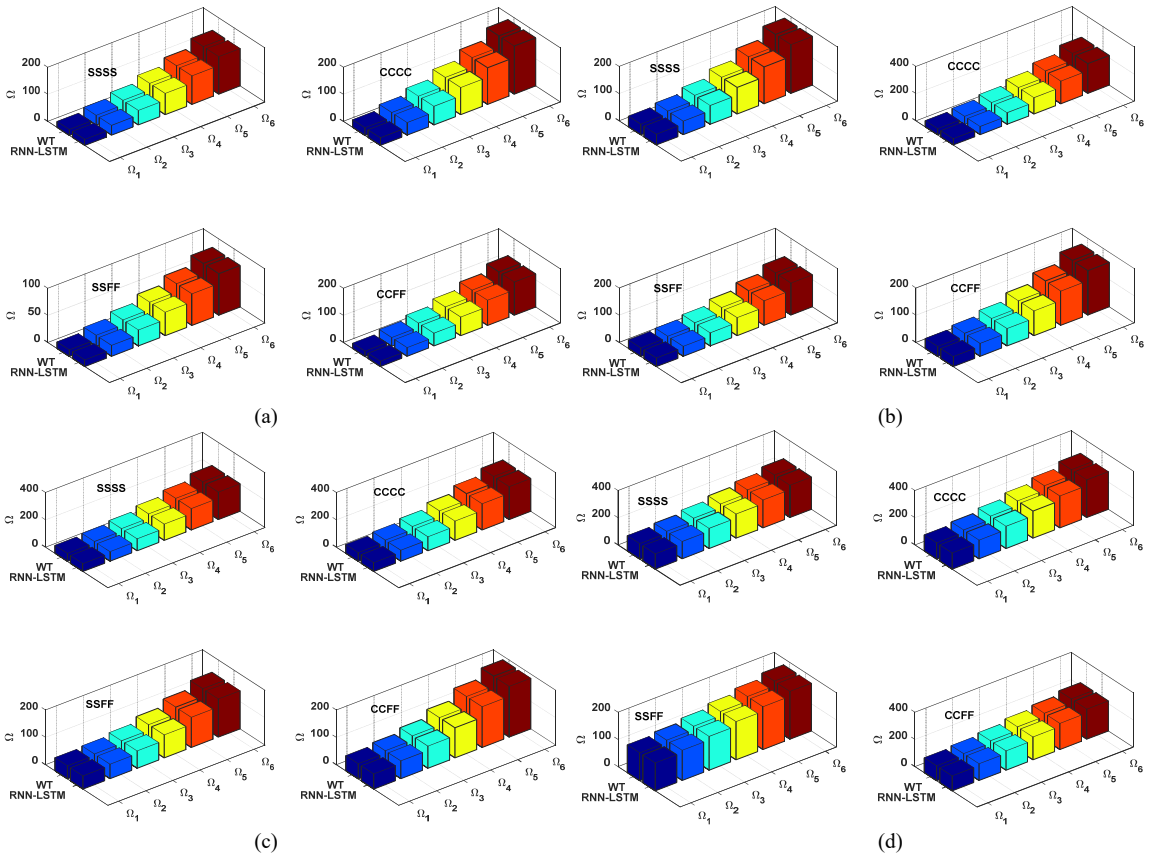

Fig. 14. Comparison between the WT data and RNN-LSTM predicted data for $K_T = 50$. (a) $\phi = 0°$; (b) $\phi = 30°$; (c) $\phi = 45°$; (d) $\phi = 60°$.

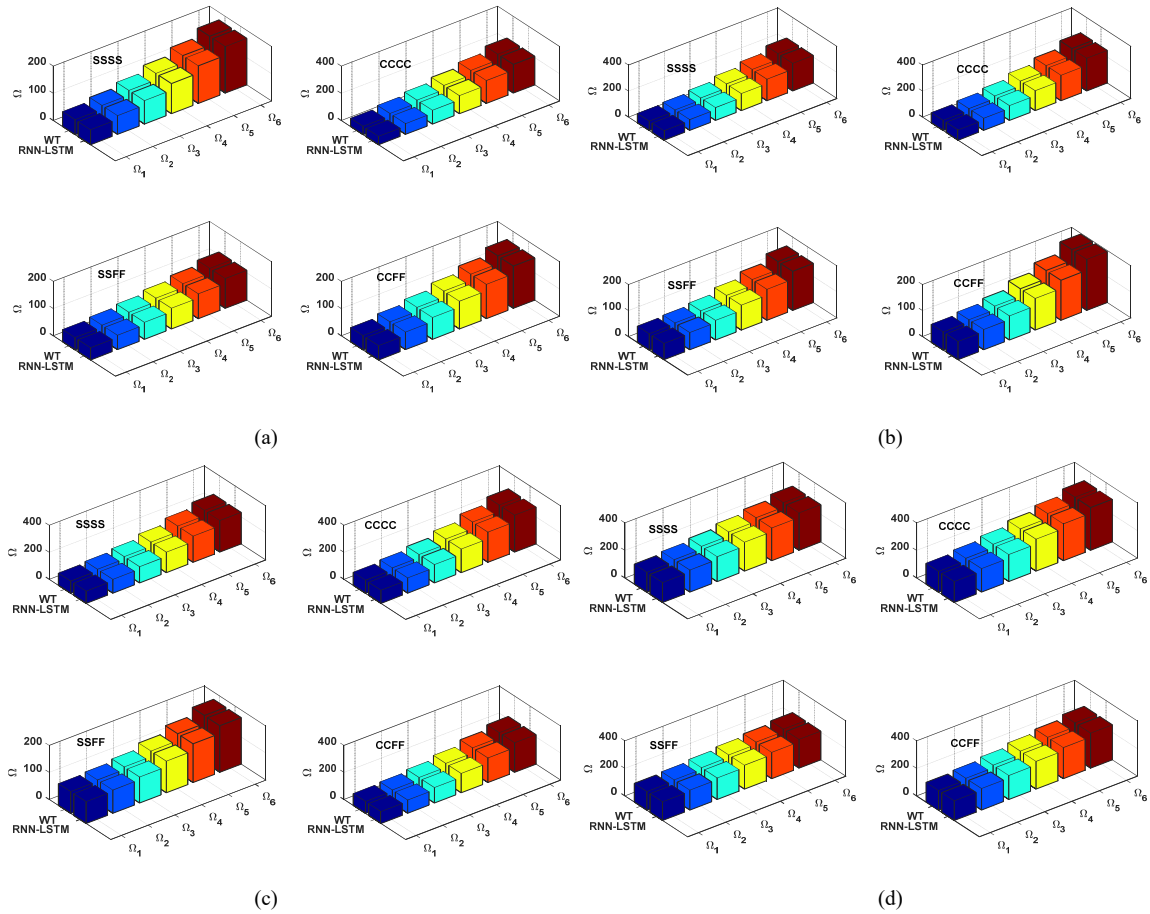

Fig. 15. Comparison between the WT data and RNN-LSTM predicted data for $K_T = 750$. (a) $\phi = 0°$; (b) $\phi = 30°$; (c) $\phi = 45°$; (d) $\phi = 60°$.

C. RNN-LSTM Performance

We can see the performance of the new RNN-LSTM model in Table IV and Fig. 12. We calculated the MSE and prediction accuracy for Ω using Eq. (21) as follow:

$$MSE = \sum((\Omega)_{NN} - \Omega)^2/n \quad (21)$$

where $(\Omega)_{NN}$ is Predicted Ω values, and n is Number of RNN-LSTM data

According to Table III and Fig. 12, the training dataset shows an MSE of $7.2\ E-5$ and an accuracy of 99.7%. On the other hand, the validation dataset has an MSE of $6.2\ E-5$ and a slightly better accuracy of 99.8%. These results really highlight that our RNN-LSTM does a great job in predicting, proving it's effective and reliable for modeling the natural frequency of NCP.

TABLE IV. MSE AND ACCURACY VALUES

Data	MSE	Accuracy (%)
Training	7.2 E−5	99.7
Validating	6.2 E−5	99.8

D. RNN-LSTM Predicting Results

In this part, we successfully hit the main goal of using the RNN-LSTM to predict how the NCP reacts to vibrations with different K_T. We looked at seven different K_T values across four common BCs setups: SSSS, CCCC, SSFF, and CCFF. We'll find the RNN-LSTM predictions for the first six natural frequencies of the NCP—where the $\beta = 0.5$ and $\Delta = 0.5$—in Fig. 16.

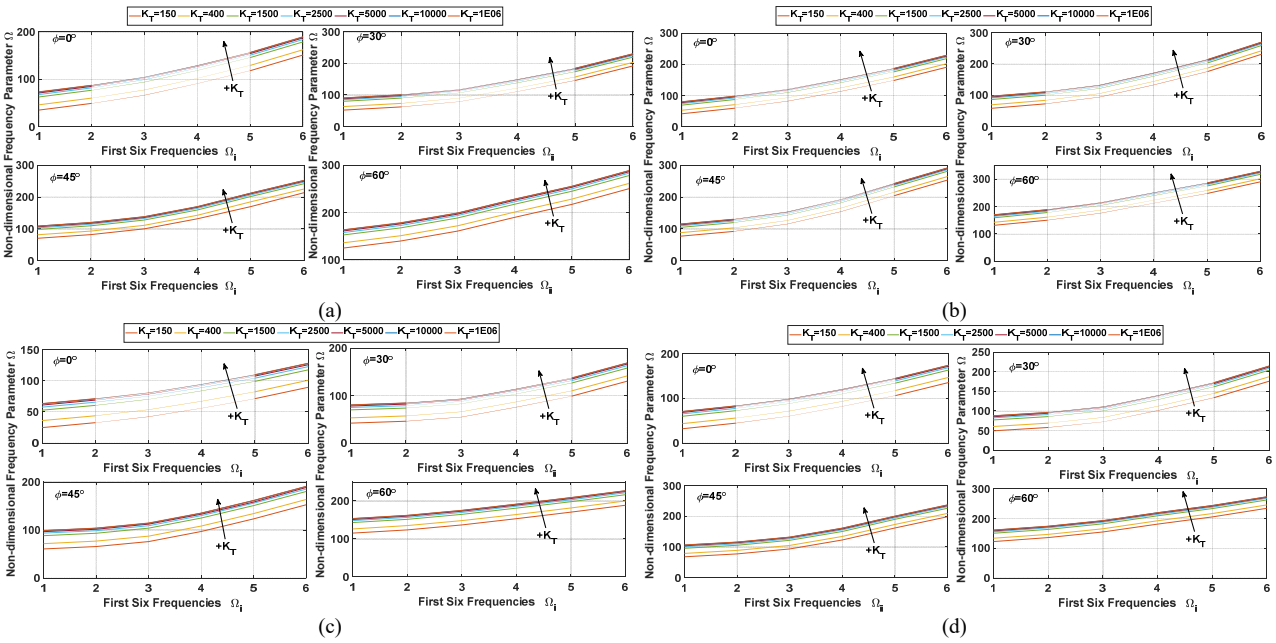

Fig. 16. The CNN predicted results of Ω. (a) SSSS; (b) CCCC; (c) SSFF; (d) CCFF.

Fig. 16 highlights how IES affects the natural frequency of NCP. The figure clearly shows that as the K_T rises, the first six natural frequencies all increase, no matter the skew angle ϕ or the type of BCs. It's interesting to note that at lower K_T values, these frequencies jump up significantly, but at higher values, the impact of the IES seems to fade away.

Looking at the skew angles ϕ, the fully clamped (CCCC) plates have the highest natural frequencies, while the semi-simply supported (SSFF) plates come in lowest. The other BCs—simply supported on all edges (SSSS) and clamped on two edges with free edges (CCFF)—sit somewhere in between. Plus, the skew angle ϕ greatly affects the Ω. As the ϕ increases, Ω does too, which suggests that the plate's angular geometry plays a key role in its vibrational features.

V. CONCLUSION

We combined the WT method with an AI algorithm to analyze the natural frequency of an NCP that has nonlinear geometry of variable thickness profile and skew in one of side, and IES with a different K_T, using BFRP laminate for the plate. To check how accurate and reliable our technique was, we did a convergence study where we compared our findings with existing literature, which helped confirm our method's credibility. Still, the approach we used can be quite computationally heavy since it involves a lot of calculations and iterations. This makes it less ideal for quickly and efficiently extracting natural frequency. To tackle this issue, we created a new RNN-LSTM model aimed at learning and testing the features of natural frequency, effectively capturing crucial information about the mode shapes of NCP. We also looked into how factors like β, Δ, ϕ, and K_T influenced the predicted Ω under four different support scenarios: SSSS, CCCC, SSFF, and CCFF. From the results predicted by both the WT and our RNN-LSTM model, it's clear that the RNN-LSTM predicted Ω aligns really well with the results from the WT method, boasting training and validation accuracies of 99.7% and 99.8%, respectively. Future work should focus on the experimental validation or real

structure applications (e.g., BFRP plates or panels in aerospace or civil engineering), incorporating additional data sources, enhancing wavelet transform, employing advanced deep learning techniques, and fostering industry collaboration to further improve and standardize SHM.

CONFLICT OF INTEREST

The authors declare no conflict of interest.

REFERENCES

[1] W. A. Altabey, S. A. Kouritem, and M. A. Al-Moghazy, "Apply frequency response function schemes for damage detection in composite nanoscale-pipes under transient conditions," *J. Nano-Structures & Nano-Objects*, vol. 39, 101259, 2024. https://doi.org/10.1016/j.nanoso.2024.101259

[2] W. A. Altabey, "The fatigue damage monitoring of composite pipeline based on frequency domain analysis of electrical capacitance sensor system measurements," *International Journal of Lightweight Materials and Manufacture*, vol. 8, no. 6, pp. 779–792, 2025. https://doi.org/10.1016/j.ijlmm.2025.06.002

[3] Z. Liping, W. Hong, and W. A. Altabey, "Bridges damage assessment techniques improvement through machine learning algorithm," in *Proc. International Conf. on Advances in Civil and Ecological Engineering Research*, 2024, vol. 336, pp. 82–92. https://doi.org/10.1007/978-981-99-5716-3_6

[4] Y. Xu, A. Yesus, J. Li *et al.,* "A new technology for structural health monitoring based on lightweight wireless self-powered sensing equipment," in *Proc. International Conf. on Advances in Civil and Ecological Engineering Research*, 2025, pp. 219–231. https://doi.org/10.1007/978-981-96-1627-5_18

[5] W. A. Altabey, "The laminated pipeline material delamination identification based on artificial intelligence schemes," *Advances in Transdisciplinary Engineering*, vol. 58, pp. 827–834, 2024. https://doi.org/10.3233/ATDE240713

[6] W. A. Altabey, "An artificial intelligence-based scheme for structural health monitoring in CFRE laminated composite plates under spectrum fatigue loading," *Structural Durability and Health Monitoring*, vol. 19, no. 5, pp. 1145–1165, 2025. https://doi.org/10.32604/sdhm.2025.068922

[7] G. Dangui, W. Hong, and W. A. Altabey, "Monitoring of bridges damage based on the system transfer function maps from sensors datasets," in *Proc. International Conf. on Advances in Civil and Ecological Engineering Research*, 2024, vol. 336, pp. 71–81. https://doi.org/10.1007/978-981-99-5716-3_5

[8] X. Jie, C. Zhifang, W. Hong *et al.,* "A novel cleaning robot for urban expressway applications: Design and evaluation," in *Proc. International Conf. on Advances in Civil and Ecological Engineering Research*, 2025, vol. 575, pp. 149–159. https://doi.org/10.1007/978-981-96-1627-5_13

[9] W. A. Altabey and M. Noori, "A mathematical modeling of BFRP laminated composite double-chamber mufflers based acoustic transmission loss optimization," in *Proc. the International Conf. of Steel and Composite for Engineering Structures*, 2024, vol. 486, pp. 54–65. https://doi.org/10.1007/978-3-031-57224-1_6

[10] Z. Sabir, G. Chen, and M. Mao, "Lightweight monitoring technology for traffic infrastructure based on wireless low-power sensing devices," in *Proc. the 6th International Conf. on Advances in Civil and Ecological Engineering Research*, 2025, vol. 575, pp. 137–147. https://doi.org/10.1007/978-981-96-1627-5_12

[11] J. Meng, W. Hong, A. F. Ba *et al.,* "Intelligence approach for road crack detection based on real-world measurement," in *Proc. the 4th International Civil Engineering and Architecture Conf.*, 2025, vol. 534, pp. 83–96. https://doi.org/10.1007/978-981-97-5477-9_7

[12] W. Hong, X. Jia, A. Silik *et al.,* "Intelligent monitoring and vision based vibration measurement on bridges," in *Proc. of the 4th International Civil Engineering and Architecture Conf.*, 2025, vol. 534, pp. 3–14. https://doi.org/10.1007/978-981-97-5477-9_1

[13] Z. Runqiu, L. Tinglin, W. Hong *et al.,* "Machine vision approach of bridges crack identification based on the fusion of UAV vision and LiDAR," in *Proc. of the 4th International Civil Engineering and Architecture Conf.*, 2025, vol. 534, pp. 39–50. https://doi.org/10.1007/978-981-97-5477-9_4

[14] W. A. Al-Tabey, "Vibration analysis of laminated composite variable thickness plate using finite strip transition matrix technique and MATLAB verifications," in *MATLAB Applications for the Practical Engineer*, IntechOpen, 2014, pp. 283–620. http://dx.doi.org/10.5772/57384

[15] Z. Chen, H. Li, W. Hong *et al.,* "Transformative insights into traffic prediction for intelligent transportation systems," *Advances in Transdisciplinary Engineering*, vol. 72, pp. 446–458, 2025. https://doi.org/ 10.3233/ATDE250444

[16] S. Bouadjadja, A. Tati, and B. Guerira, "Analytical and experimental investigations on large deflection analysis of composite cantilever beams," *Mech. Adv. Mater. Struct.,* vol. 29, pp. 118–126, 2020.

[17] Q. Cheng, Q. M. Wang, and Z. Lv, "Theoretical and experiment optimization research of a frequency up-converted piezoelectric energy harvester based on impact and magnetic force," *Eng. Res. Express*, vol. 6, 035314, 2024.

[18] H. Wu, S. Kitipornchai, and J. Yang, "Thermal buckling and postbuckling of functionally graded graphene nanocomposite plates," *Mater. Des.,* vol. 132, pp. 430–441, 2017.

[19] X. Guo, B. Zhang, D. Cao *et al.,* "Influence of nonlinear terms on dynamical behavior of graphene reinforced laminated composite plates," *Appl. Math. Model.*, vol. 78, pp. 169–184, 2020.

[20] N. Van Viet, W. Zaki, and R. Umer, "Bending theory for laminated composite cantilever beams with multiple embedded shape memory alloy layers," *J. Intell. Mater. Syst. Struct.,* vol. 30, pp. 1549–1568, 2019.

[21] L. Jun, L. Xiaobin, and H. Hongxing, "Free vibration analysis of third-order shear deformable composite beams using dynamic stiffness method," *Arch. Appl. Mech.,* vol. 79, pp. 1083–1098, 2009.

[22] M. Amabili, G. Ferrari, M. H. Ghayesh *et al.,* "Nonlinear vibrations and viscoelasticity of a self-healing composite cantilever beam: Theory and experiments," *Compos. Struct.,* vol. 294, 115741, 2022.

[23] W. Zhang, M. H. Zhao, and X. Y. Guo, "Nonlinear responses of a symmetric cross-ply composite laminated cantilever rectangular plate under in-plane and moment excitations," *Compos. Struct.,* vol. 100, pp. 554–565, 2013.

[24] X. Liu and L. Sun, "Chaotic vibration control of a composite cantilever beam," *Sci. Rep.*, vol. 13, no. 1, 17946, 2023.

[25] X. Guo, P. Jiang, and D. Cao, "Influence of piezoelectric performance on nonlinear dynamic characteristics of MFC shells," *Complexity*, vol. 2019, no. 1, 1970248, 2019.

[26] W. Zhang, L. L. Ren, Y. F. Zhang *et al.,* "Chaotic snap-through vibrations of bistable asymmetric deployable composite laminated cantilever shell under foundation excitation and application to morphing wing," *Compos. Struct.*, vol. 343, 118261, 2024.

[27] H. Teymouri and H. Biglari, "Elastodynamic Green's functions for sandwich panels with aluminum foam core and transversely isotropic face sheets using potential functions method," *Engineering Analysis with Boundary Elements*, vol. 160, pp. 258–272, 2024. https://doi.org/10.1016/j.enganabound.2023.12.033

[28] L. Sun, X. D. Li, and X. Liu, "Control of large amplitude limit cycle of a multi-dimensional nonlinear dynamic system of a composite cantilever beam," *Sci. Rep.*, vol. 14, no. 1, 10771, 2024.

[29] C. Qi, F. Gao, H. X. Li *et al.,* "A neural network-based distributed parameter model identification approach for microcantilever," *Proc. the Institution of Mechanical Engineers, Part C: Journal of Mechanical Engineering Science*, vol. 230, no. 20, pp. 3663–3676, 2015.

[30] A. Subramanian and S. Mahadevan, "Bayesian estimation of discrepancy in dynamics model prediction," *Mech. Syst. Signal Process.*, vol. 123, pp. 351–368, 2019.

[31] Q. Teng and L. Zhang, "Data driven nonlinear dynamical systems identification using multi-step CLDNN," *AIP Adv.*, vol. 9, no. 8, 085311, 2019.

[32] R. Cestnik and M. Abel, "Inferring the dynamics of oscillatory systems using recurrent neural networks," *Chaos: An Interdisciplinary Journal of Nonlinear Science*, vol. 29, no. 6, 063128, 2019.

[33] B. Huang, H. Zheng, X. Guo *et al.,* "A novel model based on da-rnn network and skip gated recurrent neural network for periodic time series forecasting," *Sustainability*, vol. 14, no. 326, 2022.

[34] G. Uribarri and G. B. Mindlin, "Dynamical time series embeddings in recurrent neural networks," *Chaos, Solitons & Fractals*, vol. 154, 111612, 2022.

[35] H. V. Dudukcu, M. Taskiran, Z. G. C. Taskiran *et al.,* "Temporal convolutional networks with RNN approach for chaotic time series prediction," *Appl. Soft Comput.*, vol. 133, 109945, 2023.
[36] M. Sangiorgio, F. Dercole, and G. Guariso, "Forecasting of noisy chaotic systems with deep neural networks," *Chaos, Solitons & Fractals*, vol. 153, 111570, 2021.
[37] Y. Sun, L. Zhang, and M. Yao, "Chaotic time series prediction of nonlinear systems based on various neural network models," *Chaos, Solitons & Fractals*, vol. 175, 113971, 2023.
[38] L. Wang, L. Dai, and L. Sun, "ConvLSTM-based spatiotemporal and temporal processing models for chaotic vibration prediction of a microbeam," *Communications in Nonlinear Science and Numerical Simulation*, vol. 140, 108411, 2025
[39] S. Chakraverty, *Vibration of Plates*, FL, USA: CRC Press, 2009.
[40] W. A. Altabey, "Innovative intelligent and expert system of bridges damage identification via wavelet packet energy curvature difference method integrated with artificial intelligence algorithms," *Sound and Vibration*, vol. 59, no. 2, 2372, 2025. https://doi.org/10.59400/sv2372
[41] W. A. Altabey, "The advanced structural health monitoring by non-destructive self-powered wireless lightweight sensor," *Structural Durability & Health Monitoring*, vol. 19, no. 6, pp. 1529–1545, 2025. https://doi.org/10.32604/sdhm.2025.069003
[42] W. A. Altabey, "Improvement of adaptive vibration isolators based on magnetorheological elastomer materials," *Advances in Transdisciplinary Engineering*, vol. 58, pp. 284–290, 2024. https://doi.org/10.3233/ATDE240636
[43] M. R. Ashory M. M. Khatibi, M. Jafari *et al.,* "Determination of mode shapes using wavelet transform of free vibration data," *J. Archive of Applied Mechanics*, vol. 83, pp. 907–921, 2013.
[44] F. J. Miranda, "Wavelet analysis of lightning return stroke," *J. Atmospheric and Solar-Terrestrial Physics*, vol. 70, no. 11–12, pp. 1401–1407, 2008.
[45] W. A. Altabey, "A novel framework to identify delamination location/size in bfrp pipe based on Convolutional Neural Network (CNN) algorithm hybrid with capacitive sensors," *International Journal of Lightweight Materials and Manufacture*, vol. 8, no. 3, pp. 393–401, 2025. https://doi.org/10.1016/j.ijlmm.2024.12.002
[46] B. Jang, M. Kim, and G. Harerimana, "Bi-LSTM model to increase accuracy in text classification: Combining word2vec CNN and attention mechanism," *Appl Sci.,* vol. 10, 2020. https://doi.org/10.3390/app10175841
[47] P. K. Diederik and B. Jimmy, "Adam: A method for stochastic optimization," arXiv preprint, arXiv: 1412.6980, 2014.
[48] R. Martinez-Cantin, "Bayesopt: A bayesian optimization library for nonlinear optimization, experimental design and bandits," *Machine Learning Research*, vol. 15, no. 1, pp. 3735–3739, 2014.
[49] H. Zhifang, W. Hong, and W. A. Altabey, "A digital simulation for bridges management by integrating LiDAR scanning and recurrent neural network with long short-term memory blocks (RNN-LSTM)," *Advances in Transdisciplinary Engineering*, vol. 72, pp. 918–927, 2025. https://doi.org/10.3233/ATDE250492
[50] F. Hutter, H. H. Hoos, and K. Leyton-Brown, "Sequential model-based optimization for general algorithm configuration," in *Proc. International Conf. on Learning And Intelligent Optimization*, 2011, vol. 6683, pp. 507–523. https://doi.org/10.1007/978-3-642-25566-3_40
[51] J. Bergstra, R. Bardenet, Y. Bengio *et al.,* "Algorithms for hyper-parameter optimization," *Advances in Neural Information Processing Systems*, pp. 2546–2554, 2011.
[52] J. Bergstra, D. Yamins, and D. Cox, "Making a science of model search: Hyperparameter optimization in hundreds of dimensions for vision architectures," in *Proc. the 30th International Conf. on Machine Learning*, Atlanta, USA, 2013, pp. 115–123.